Development of Multi-scale Models for Transport Processes Involving Catalytic Reactions in SOFCs

Sundén, Bengt; Yuan, Jinliang

[Link to publication](#)

Development of Multi-scale Models for Transport Processes Involving Catalytic Reactions in SOFCs

Bengt Sundén and Jinliang Yuan

Department of Energy Sciences, Lund University
Box 118, 22100 Lund, Sweden

ABSTRACT

Several physical phenomena appear in anode-supported solid oxide fuel cells (SOFCs), such as multi-component gas species/charge flow, thermal energy and mass transfer. Meanwhile, generation and consumption of gas- and surface-phase species together with electric current production are involved at the active sites in different length scales. Therefore, various reactions in SOFCs are strongly coupled with the transport processes making the physical phenomena more complicated. An effective anode is the one that correctly balances each of the transport processes and the reactions. To deeply understand the chemical-reacting transport processes in the porous anode, a fully three-dimensional numerical calculation method (CFD approach) is further developed. The considered domain includes the porous anode, fuel gas flow channel and the solid interconnects. By calculating surface-phase species, the gas-phase species/heat generation and consumption related to the internal reforming reactions and the electrochemical reactions have been employed. The variable thermal-physical properties and transport parameters of the fuel gas mixture have also been taken into account. Furthermore, the heat transfer due to the fuel gas diffusion is implemented into the energy balance based on multi-component diffusion models. A multi-step heterogeneous steam reaction scheme based on the micro and detailed reaction mechanisms of Ni catalyst is employed in this study. The surface reactions include 42 irreversible elementary ones, and they account for the steam reforming, the water-gas shift reforming and Boudouard reactions. This microscopic reaction model describes the adsorption and desorption reactions of 6 gas-phase species (H_2, CO, CH_4, CO_2, H_2O and O_2) and surface reactions of 12 surface-adsorbed species (Ni_s, H_s, O_s, OH_s, HCO_s, CH_s, CH_{2s}, CH_{3s}, CH_{4s}, CO_s, CO_{2s}, H_2O_s). Simulation results are presented and discussed in terms of the gas-phase species and temperature distributions, the chemical reaction rates of the gas- and surface chemical species, the catalyst surface coverage and the effects on the transport processes.

1. INTRODUCTION

High temperature solid oxide fuel cells (SOFCs), with the advantages of high efficiencies, environmental friendliness and flexibility of usable fuel types, have been considered as one of the most promising technologies for electricity energy generation. Many variations of SOFC designs are possible, such as tubular, planar and monolithic. The planar SOFCs have several advantages, such as higher power density, compactness, and simple to fabricate and manufacture into various configurations [1]. It is a fact that the requirement of high temperature gas seals, internal stresses in

cell components is very critical for SOFCs development [1]. One of the new trends is to reduce the operating temperature of SOFCs to an intermediate range (from 1000^oC to around 800^oC) by employing a thick porous layer (1.5-2 mm) as the supporting structure [2-5]. The transport rate of fuel gases in the porous anode is controlled by various parameters, such as porous microstructure, pressure gradient between the fuel flow channel and the porous anode, gas composition and inlet conditions, etc. [6,7]. In general, the porous electrodes are multiphase materials, e.g., transport of reactants/products, and electrons. The porous anodes provide active sites for internal reforming reactions in which the solid portion is either dispersed within a fluid medium or has a fluid network within. For the first case, the fluid medium occupies pores and the characteristic length is the diameter of the pores, while the particle size is the characteristic length if the solid fraction of the porous media is dispersed. In addition to pore diameter, or particle size, there are two more characteristics of flow paths in porous media, i.e., porosity and tortuosity. As an example, Ni-doped YSZ (yttria stabilized zirconia) materials are typically employed as the porous anodes in SOFCs. It is revealed that the pore or voids of diameter is less than 0.3 μm, and porosities ranging between 0.3-0.6, while the particle diameter is about 1 μm for both spherical particles and sintered metal beads [8-10].

For the case of pure hydrogen being employed as a fuel, part of H_2 is consumed while water vapor (H_2O) is generated during the electrochemical reaction. If methane is used as the fuel, internal reforming reactions within SOFC anodes enable the conversion of the methane into H_2 and CO. It is a fact that the heat required to keep internal steam reforming can be provided by the electrochemical reactions in SOFCs. Several benefits are expected if internal steam reforming of hydrocarbon fuels is employed. Close coupling of the internal reforming and the electrochemical reactions at the anode gives also good heat transfer. Furthermore, H_2 and CO are utilized by the cells as soon as they are produced by the reforming reaction, and the steam produced by the electrochemical reaction can be used in the reforming reaction as well [9, 10].

To deeply understand the effects of design and operating parameters on the chemical-reacting transport processes in the porous anode, a fully three-dimensional numerical calculation procedure (CFD approach) is further developed. The considered domain includes the porous anode, fuel gas flow channel and the solid interconnects. By calculating surface-phase species, the gas-phase species /heat generation and consumption related to the microscopically internal reforming and the electrochemical reactions have been identified and employed in the study. The variable thermal-physical properties and transport parameters of the fuel gas mixture have also been taken into account. Furthermore, the heat transfer due to the fuel gas diffusion is implemented into the energy balance based on multi-component diffusion models. One of the objectives of this study is to develop such an approach to understand effects on various transport processes coupled with the catalytic reactions in the anode channels of ITSOFCs.

2. MODELS AND FORMULATIONS

Structure of a unit cell and a schematic drawing of the anode are shown in Figs. 1a and b, respectively. The *U*, *V*, and *W* in Fig. 1b are the velocity components in the *x*, *y*, *z* directions, respectively. In this study, the porous anode layer is assumed to be homogeneous and characterized by effective parameters and the fuel gas-phase species in the porous anode are in thermal equilibrium with the solid matrix. The electrochemical reaction appears at the three-phase boundary (TPB) between the electrolyte and the porous layer, i.e., the bottom surface in Fig. 1b, while the internal reforming reactions appear in the porous anode. A constant fuel flow rate $U=U_{in}$ with a mole fraction of the mixed fuel gas is specified at the inlet of the fuel gas flow channel, while $U=0$ is specified at the inlet for interconnector (or current connector) and the porous anode. Only the right half of the channel is considered by imposing symmetry conditions on the mid-plane.
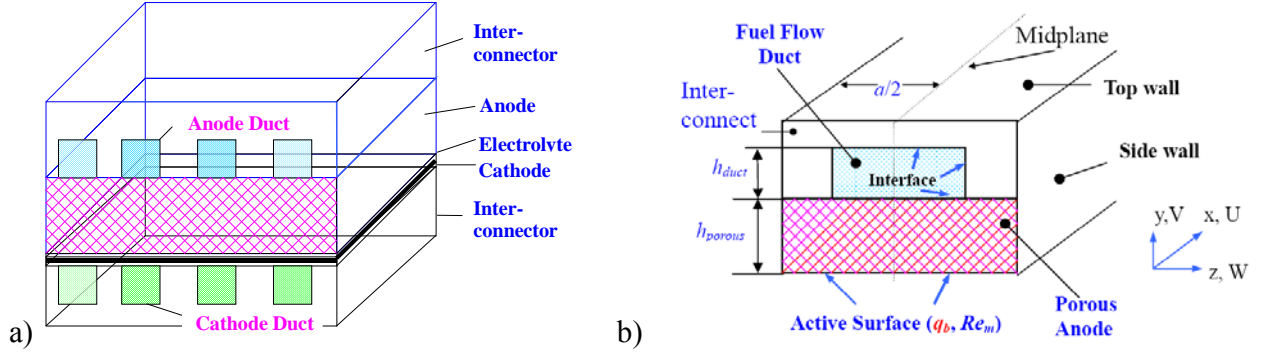
Figure 1. a) Structure of a unit cell; b) schematic drawing of a composite anode domain in ITSOFCs.

2.1. Chemical Reactions and Reaction Kinetics
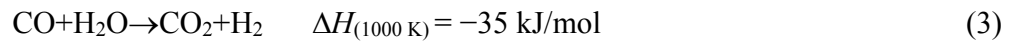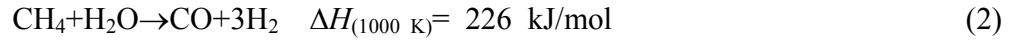
In Ni/YSZ anode-supported SOFCs, the porous anode is usually on the order of a millimeter thick, while the dense electrolyte and the cathode are of the order of 10 μm thick. The electrochemical reactions to generate electricity by the oxidation of H_2 are confined to the very thin TPB:

$$H_2 + O^{2-} \rightarrow H_2O + 2e^- \quad \Delta H_{(1000\ K)} = -248 \text{ kJ/mol} \tag{1}$$
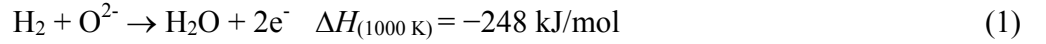
As revealed in [8], the electrochemical oxidation rate of H_2 is twice or several times higher than that of CO, the contribution of CO oxidation to the cell performance (the total current density) and effects on the transport processes may be small and are neglected in this study. The above reactions produce a significant amount of water and heat at the anode/electrolyte interface during operation.

It should be mentioned that the majority of the porous anode serves non-electrochemical purpose. Among others, Ni serves as a catalyst for the methane reforming reactions. Methane and carbon monoxide can be internally reformed into H_2 by the following global reactions:

$$CH_4 + H_2O \rightarrow CO + 3H_2 \quad \Delta H_{(1000\ K)} = 226 \text{ kJ/mol} \tag{2}$$

$$CO + H_2O \rightarrow CO_2 + H_2 \quad \Delta H_{(1000\ K)} = -35 \text{ kJ/mol} \tag{3}$$

Equation (2) is internal steam reforming reaction, while Eq. (3) is usually referred to as water-gas shift reaction. It should be mentioned that the steam reforming reaction is endothermic and the overall balance of the reaction requires net heat input by the electrochemical reactions.

It is a fact that gas-phase species of H_2O and CO_2 are formed via catalytic and electrochemical reactions inside the porous anode. The internal reforming and the water-gas shift reforming reactions have been usually considered to be global kinetics processes, and assumed to be locally equilibrated, and then modeled by empirical and global reactions without involving elementary catalytic reactions and surface intermediates. For instance, the global kinetics of the methane reforming reactions reads as [9]:

$$k^+ = k_0 F(p_i) exp\left(-\frac{E_a}{\Re T}\right) \tag{4}$$

where $\Re$ is the universal gas constant with units J/(mol K), F the function of the gas-phase species partial pressure, while E_a stands for the activation energy, k_0 the pre-exponential constant. It is revealed that the first order kinetic expression is considered typical of direct internal reforming

reactions in SOFC performance [9, 10]. The backward kinetics k_r^- and k_s^- are usually determined based on the equilibrium constants K_e for the two reactions,

$$K_{er} = \frac{k_r^+}{k_r^-}; K_{es} = \frac{k_s^+}{k_s^-}$$

(5)

which are functions of temperature given by the empirical equations [11]. In recent years, an increasing number of heterogeneous catalysis systems have been successfully described by mechanistic schemes based on molecular behavior at the catalytic surface [12-15]. In this study, a multi-step heterogeneous steam reforming reaction model based on the microscopic and detailed reaction mechanisms of Ni/YSZ has been implemented. The catalytic reaction sheme in the appendix A includes 42 irreversible elementary ones, which were evaluated for temperatures between 220 and 1700°C, and accounts for the steam reforming, the water-gas shift reforming and Boudouard reactions [15]. This microscopic submodel describes the adsorption and desorption reactions of 6 gas-phase species (H_2, CO, CH_4, CO_2, H_2O and O_2) and the catalytic reactions of 12 surface adsorbed species (Ni_s, H_s, O_s, OH_s, HCO_s, CH_s, CH_{2s}, CH_{3s}, CH_{4s}, CO_s, CO_{2s}, H_2O_s). It is clear that the gas-phase species are coupled with the chemical reaction rates of both gas- and surface species, the catalyst surface coverage, and further affect the transport processes.

2.2. Governing Equations and Source Terms for the Transport Processes
The governing equations to be solved are the continuity, momentum, energy and gas-phase species equations, as listed in Table 1.

Table 1. Governing equations and relevant source terms.

	Governing equations	Source terms	Subdomain
Continuity equation	$\nabla \bullet (\rho_{\text{eff}} \mathbf{v}) = S_m$	$S_m = (J_{H_2} + J_{H_2O}) \dfrac{A_{\text{active}}}{V}$ $= (-\dfrac{i_{H_2}}{2F} M_{H_2} + \dfrac{i_{H_2}}{2F} M_{H_2O}) \dfrac{A_{\text{active}}}{V}$	the bottom surface in Fig. 1b
Momentum equation	$\nabla \bullet (\rho_{\text{eff}} \mathbf{vv}) = -\nabla P + \nabla \bullet (\mu_{\text{eff}} \nabla \mathbf{v}) + S_{\text{di}}$	$S_{\text{di}} = -(\mu_{\text{eff}} \mathbf{V} / \beta)$	Porous anode
Gas-phase species equation	$\nabla \bullet (\rho_{\text{eff}} \mathbf{V} Y_i) = \nabla \dot{m}_i + S_{s,i}$	$S_{s,i} = \left(\sum\limits_{j=1}^{Kr} v_{ij} k_j \prod\limits_{i=1}^{Kg+Ks} [X_i]^{v'_{ij}} \right) M_i$	Porous anode
Energy equation	$\rho_{\text{eff}} c_{p,\text{eff}} \nabla \bullet (\mathbf{v} T) = \nabla \bullet (k_{\text{eff}} \nabla T$ $- \sum\limits_{i=1}^{n} \dot{m}_i h_i) + S_T$	$S_T = \sum\limits_i R_i \Delta h_{\text{reaction},i}$	Porous anode

The inclusion of the source term S_{di} allows the momentum equation to be valid for both the porous layer and the fuel gas flow channel, i.e., the source term is zero in the fuel gas flow channel, because the permeability β is infinite. The momentum equation then reduces to the regular Navier-Stokes equation. For the porous anode, the source term S_{di} is not zero, and the momentum equation with the non-zero source term can be regarded as a generalized Darcy model [10].

The gas-phase species conservation equations are formulated in a general form, where Y_i is the mass fraction of the ith fuel gas species, $\dot{m}_i$ represents the mass diffusive flux of gas-phase species in units of kg/(m^2 s), and $S_{s,i}$ the production/consumption rate of the ith fuel species. This equation is solved for 6 gas-phase species, i.e., H_2, O_2, CH_4, H_2O, CO_2 and CO, respectively. In the current work the

internal reforming reactions are evaluated by a multi-step microscopic reaction mechanism for YSZ/Ni catalysts. As shown in the appendix A, this chemistry consists of 42 reactions involving the 6 gas-phase species coupled by other 12 surface adsorbed species (Ni_s, H_s, O_s, OH_s, HCO_s, CH_s, CH_{2s}, CH_{3s}, CH_{4s}, CO_s, CO_{2s}, H_2O_s). It is found that most of the reactions in the appendix A can be expressed in Arrhenius rate form, and some are dependent on the surface coverage of CO_s species, i.e., ε_{CO_s} in the reactions 12, 20, 21, 23 in the appendix A. The reaction rate constants are expressed as [15]

$$k_j = A_j T^{\beta_j} \exp(-\frac{E_{aj}}{RT}) \prod_{k=1}^{K_s} \theta_k^{\mu_{kj}} \exp(-\frac{\varepsilon_{kj}\theta_k}{RT})$$

(6)

where k_j is the rate constant for the jth reaction in the appendix A, μ_{kj} and ε_{kj} are the parameters modeling the coverage dependence on the rate constant, while θ_k is the surface coverage of the kth species following the conservation law, $\sum \theta_k = 1$. The production/consumption rates of each gas-phase species, $S_{s,i}$ in the Table 1, are the source terms to the species equations. K_r is the number of reactions, K_g and K_s represent the number of the gas-phase species and the surface species, respectively; v_{ij} is the difference in stochiometric coefficients of the products and reactants, v_{ij}' the stochiometric coefficients of the products and $[X]_i$ the concentration of the ith chemical species.

The gas-phase species concentration is evaluated as $[X_i] = \dfrac{X_i p}{R_g T \cdot 10^6}$ (mol/cm^3), and the surface-phase species concentration is $[X_i] = \theta_i \Gamma_{tot}$ (mol/cm^2), where Γ_{tot} is the total catalyst surface species including open catalyst species Ni_s. For the 6 gas-phase species K_g, the net production rate can be re-arranged to the difference between desorption/adsorption rates R_i^{des} (positive v_{ij}) and R_i^{ad} (negative v_{ij}), $S_{s,i} = R_i^{des} - R_i^{ad}$. On the other hand the 12 surface-phase species K_s are effectively immobile on length scales larger than an individual catalyst particle, and the surface species production rates are usually zero at steady-state conditions, $S_{s,i} = 0$. It should be noted that the total nickel surface is estimated from the specific surface area of the nickel catalyst (a_{NI}=1080 cm^2/cm^3).

Mass diffusion is a process leading to equalization of substance concentration or establishing an equilibrium gas distribution that results from random migration of the species. Molecular diffusion occurs as a result of thermal motion of the molecules, and proceeds at a maximum rate in gases, a lower rate in liquids, and at a still lower rate in solids [17]. In the general case, the molecular diffusion flux of the species i is proportional to the concentration gradient and diffusion coefficient. One of the significant challenges in SOFC modelling is in determining the rate at which the species diffuse and gases convect in the gas flow channels and porous electrodes. This requires knowledge of multi-component diffusion in the fuel gas flow channels, particularly in the porous layers. In the literature, the Stefan-Maxwell model is more commonly used in multi-component system, as in this study. The diffusion coefficients of species i in the fuel gas flow channel is calculated by the expression based on the binary coefficients [17]

$$D_{i,gm} = \frac{1 - X_i}{X_j / D_{ij} + X_k / D_{ik} + ...}$$

(7)

where D_A is the diffusion coefficient of the component i in the mixture with j, k, …, X_i, X_j, X_k are the molar fraction of the appropriate species, and D_{ij} and D_{ik} are the diffusion coefficients in the ij and ik binary system, respectively. It is clear that for an n component system, $n(n-1)/2$ binary diffusivities are required.

For the porous layer, molecular diffusion is predominant in the case with large pores, whose size is much bigger than the free-path of the diffusion gas molecules. In this case, the diffusion can be described as above presented for the fuel gas flow channel. Knudsen diffusion occurs in the porous layer with small pores or under low pressure when the mean free-path of molecules is smaller than the pore size, and the molecules collide with the walls more often than between themselves. In order to calculate the Knudsen diffusion flux, the coefficient $D_{i,k}$ is calculated based on the free molecule flow theory [17]:

$$D_{i,k} = \frac{2}{3} r_e v_i = \frac{2}{3} r_e \sqrt{\frac{8\Re T}{\pi M_i}} \tag{8}$$

in which r_e is the effective radius and v_i the average molecular speed of the ith fuel species. To account for the reduction in the cross-sectional area and the increased diffusion length due to the tortuous paths of real pores in the porous anode, the effective diffusion coefficient can be evaluated [11, 17]:

$$D_{i,\text{eff}} = \frac{\varepsilon}{\tau} \left(\frac{D_{i,gm} \times D_{i,k}}{D_{i,gm} + D_{i,k}} \right) \tag{9}$$

where ε is the porous anode porosity, τ tortuosity.

The energy equation balances the convected energy, the heat conduction through the solid and the fuel gas mixture (heat conduction), the energy due to fuel gas species diffusion, and a source term S_T. In which h_i is the partial enthalpy of the ith species and is obtained from [11]:

$$h_i = h_{\text{form},i} + \int_{T_0}^{T} c_{pi}(T) dT \tag{10}$$

where $h_{\text{form},i}$ is the specific enthalpy of formation of the ith fuel species at $T = T_0 = 298.15$ K. The heat source term S_T in the energy equation is associated with the steam reforming and the water-gas shift reactions. It should be noted that all thermal-physical and transport parameters with subscript eff are the effective ones, and reduce to the values of the fuel gas mixture in the fuel gas flow channel based on the fuel species composition. However, for the porous anode the effective density is simply evaluated by ρ_f of the fuel gas mixture ($H_2+O_2+CH_4+H_2O+CO_2+CO$), while, the effective transport parameters, such as thermal conductivity k_{eff} and specific heat $c_{p,\text{eff}}$, are estimated by considering the porous layer effects:

$$k_{\text{eff}} = \varepsilon k_f + (1-\varepsilon) k_s \tag{11}$$

$$c_{p,\text{eff}} = \varepsilon c_{p,f} + (1-\varepsilon) c_{p,s} \tag{12}$$

2.3. Boundary and Interface Conditions

Based on the SOFC function, typical velocities, fuel gas mass fraction/flux boundary conditions are specified at the external walls in this study. For the temperature boundary conditions, the thermal insulation is put on the walls (the top and side ones), and a constant heat flux condition is specified at the active surface, i.e.,
at the bottom wall ($y = 0$):

$$U = V\text{-}V_m = W = 0; \quad q_b = -k_{\text{eff}} \frac{\partial T}{\partial y}; \quad J_i = -\rho_{\text{eff}} D_{i,\text{eff}} \frac{\partial Y_i}{\partial y}$$

$$(i = H_2, CO \text{ and } H_2O) \text{ and } J_i = 0 \ (i = O_2, CH_4 \text{ and } CO_2) \tag{13}$$

at the top/side walls:

$$U = V = W = 0; \quad q = 0; \quad J_i = 0 \tag{14}$$

at the mid-plane ($z=a/2$):

$$\frac{\partial U}{\partial z} = \frac{\partial V}{\partial z} = W = \frac{\partial T}{\partial z} = \frac{\partial Y_i}{\partial z} = 0 \tag{15}$$

It is very interesting to point out that the thermal conditions at the top and side interfaces are implicitly obtained by thermal coupling through the top/side interfaces, while all the conditions at the bottom interface (between the fuel flow channel and the porous anode in Fig. 1) by coupling the mass, heat and species transfer. As expected, the thermal conditions at the interfaces are characterized by axially varying interface heat fluxes (or temperature gradients) and interface temperatures, due to the complex hydrodynamic and thermal transport interactions by the chemical reactions, species flux through the porous reaction layer, and the convective flows in the gas flow channel [16].

3. CFD APPROACH AND SOLUTION METHODS
A three-dimensional CFD code is further developed and employed to solve the governing equations in Table 1, together with the boundary conditions (13-15). The code is a general purpose one based on the finite-volume technique with boundary fitted coordinates for solving the differential equations. The momentum equations are solved for the velocity components on a non-staggered grid arrangement. The Rhie-Chow interpolation method is used to compute the velocity components at the control volume faces. Algorithms based on the TDMA (Tri-Diagonal Matrix Algorithm) and a modified SIP (Strongly Implicit Procedure) are employed for solving the algebraic equations. The convective terms are treated by the QUICK (Quadratic Upstream Interpolation Convective Kinematics) scheme, while the diffusive terms are treated by the central difference scheme. The SIMPLEC (Semi-Implicit Method for Pressure-Linked Equations-Consistent) algorithm handles the linkage between velocities and pressure.

As discussed above, the equations needed for the calculation are coupled by the current density, temperature, the gas/surface species concentrations via source terms and variable physical/transport properties. It should be noted that the source term in the continuity equation is zero in most of the regions, and non-zero only in the regions neighboring boundaries, where mass transfer caused by the electrochemical reaction occurs (the bottom wall in Fig. 1b). It is a fact that no gas flow is present in the solid interconnect. The continuity, momentum and species equations are then blocked out and only the heat conduction equation, derived from the energy equation, is solved for this domain. As mentioned earlier, the physical/transport properties of the fuel gas mixture are variable. These parameters depend on the position in the channel, and the gas species mass fraction and temperature as well. All the parameters are calculated and updated during iterations of the calculation.

In this study, a uniform grid point distribution in the cross section is applied. To obtain finer meshes in the entrance region of the channel, a non-uniform distribution of grid points with an expansion factor is implemented for the main flow direction. In order to evaluate the performance of the numerical method and code, test calculations considering grid sensitivity, code performance and validation were carried out. It is clear that the predictions do not change significantly in terms of fuel species distributions, when the number of grid points is increased beyond $70 \times 70 \times 50$ (70×50 for the cross section, 70 for the main flow direction).

4. RESULTS AND DISCUSSION
Parameters of ITSOFCs and the porous anode configuration from common literature are applied as a base case in this study. Channel geometries are: length of the channel $L = 20$ mm; width of the

porous layer a = 2 mm, and its thickness h_p = 2 mm; while the width of the flow channel is b = 1 mm, and its height h_d = 1 mm. Fuel gas inlet conditions are: temperature T_{in} = 800 ^{o}C, partially (30%) preformed methane/steam mixture with: Re_{in} =50, molar concentration X_{H2}:X_{CH4}:X_{CO}:X_{H2O}:X_{CO2} =0.280:0.171:0.023:0.473:0.053 [6]; In the porous layer, typical values are employed for porosity ε =0.5, tortuosity τ =3, and permeability β =2×10^{-10} m^2; The binary diffusion coefficients of the fuel species are shown in Table 2. In this study, a constant current density i = 0.6 A/cm^2 is prescribed.

Table 2. Binary diffusivity of the *i*th gas-phase species at *T*=1123.15 K, *p*=1.013 bar [4].

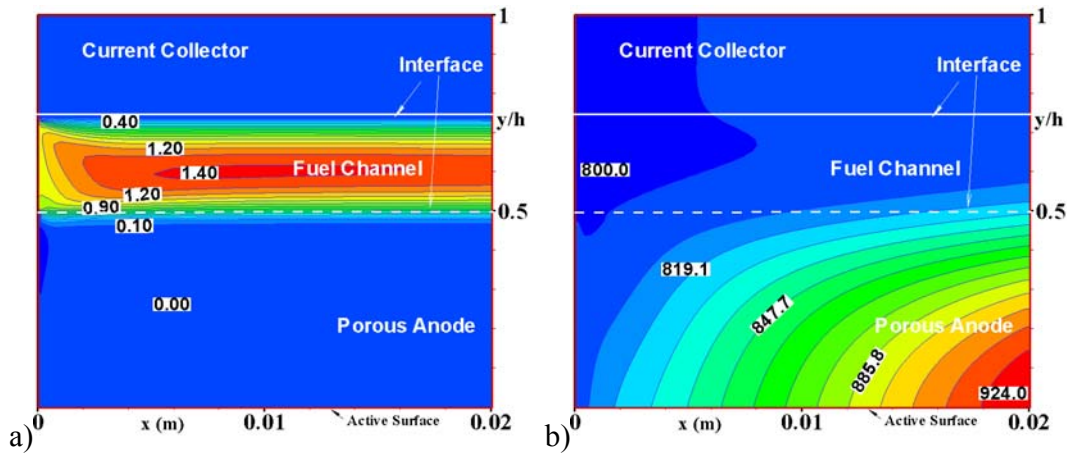| i/j	D_{ij} (m^2/s)	i/j	D_{ij} (m^2/s)
CH$_4$/CO	3.47e-05	CO/H$_2$	11.92e-05
CH$_4$/H$_2$O	4.30e-05	CO/CO$_2$	2.59e-05
CH$_4$/H$_2$	11.04e-05	H$_2$O/H$_2$	14.10e-05
CH$_4$/CO$_2$	2.88e-05	H$_2$O/CO$_2$	3.38e-05
CO/ H$_2$O	4.15e-05	H$_2$/CO$_2$	10.23e-05

Figure 2. a) Velocity (U/U_{in}); and b) temperature contours along the anode main flow direction.

As shown in Fig. 2, gas flow and heat transfer in the composite channels are affected by the catalytic reforming reactions in the porous anode layer and the electrochemical reactions close to the active surface (TPB). Due to the permeation and mass generation/consumption effects, the uniform distribution and the symmetry of the axial velocity associated with a pure forced channel flow does no longer exist, and the position of the maximum contour values shifts away from the central plane. More mass is permeated into the porous anode layer at the entrance area because the largest pressure gradient between the flow channel and the porous layer occur here. As a consequence, part of the boundary is shifted into the porous anode layer, which can be verified by a change of the boundary layer thickness close to the interface. Temperature profiles are presented in Fig. 2b. It is clear that the temperature in the porous anode increases after a certain distance downstream the entrance along the main flow direction. Moreover, the variation in temperature distribution can be identified in the vertical direction with a slightly larger value close to the active surface. These are created by the heat generation due to the electrochemical reactions close to the active surface.

The internal reforming reaction can be found in Fig. 3*a* by the methane mass fraction distribution in the anode channel, particularly in the porous anode. A large amount of CH$_4$ reacts at the interface region of the porous layer close to the fuel channel, which is reflected by a sharp decrease of the CH$_4$ mass concentration. It is found that the reactions take place more deeply into the porous anode in the most porous region, and there is a certain amount of methane which has not been reformed in both the fuel and porous anode based on this elementary reaction scheme. On the other hand, the active surface is sufficiently supplied with H$_2$ resulting from both the steam reforming and the water-gas

shift reactions. Moreover, the H_2 mass concentration is affected by the mass consumption due to the electrochemical reactions, as shown in Fig. 3b.
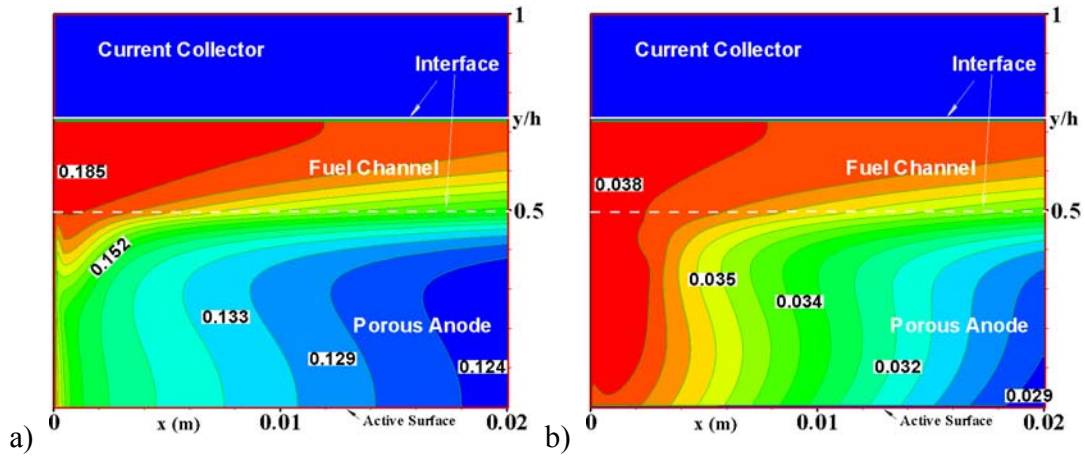

Figure 3. Gas-phase species mass concentration of: a) CH_4; and b) H_2 along main flow direction of an ITSOFC anode.
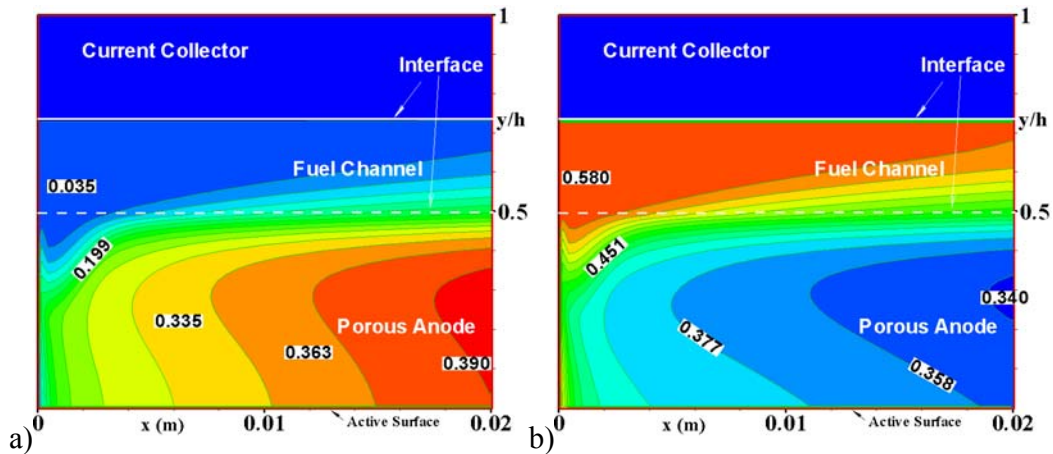

Figure 4. Gas-phase species mass concentration of: a) CO; and b) H_2O along main flow direction of an ITSOFC anode.

CO and H_2O mass fraction profiles along the main flow stream are shown in Fig. 4. It is found that there is a small CO concentration within the porous anode close to the flow channel at the entrance region, and the concentration increases along the main flow direction with big values appearing in the middle part of the porous anode from the fuel. This is so because the CO reaction rate is big in these regions, as shown below. It is observed that H_2O is consumed in the porous anode by both the steam reforming and the water-gas shift reactions. For this reason, mass fractions of H_2O decrease along the main flow direction. However, generation of H_2O by the electrochemical reactions affects the H_2O distribution as well, particularly for the area close to the active surface. A minimum value is found in the porous anode close to the channel exit.
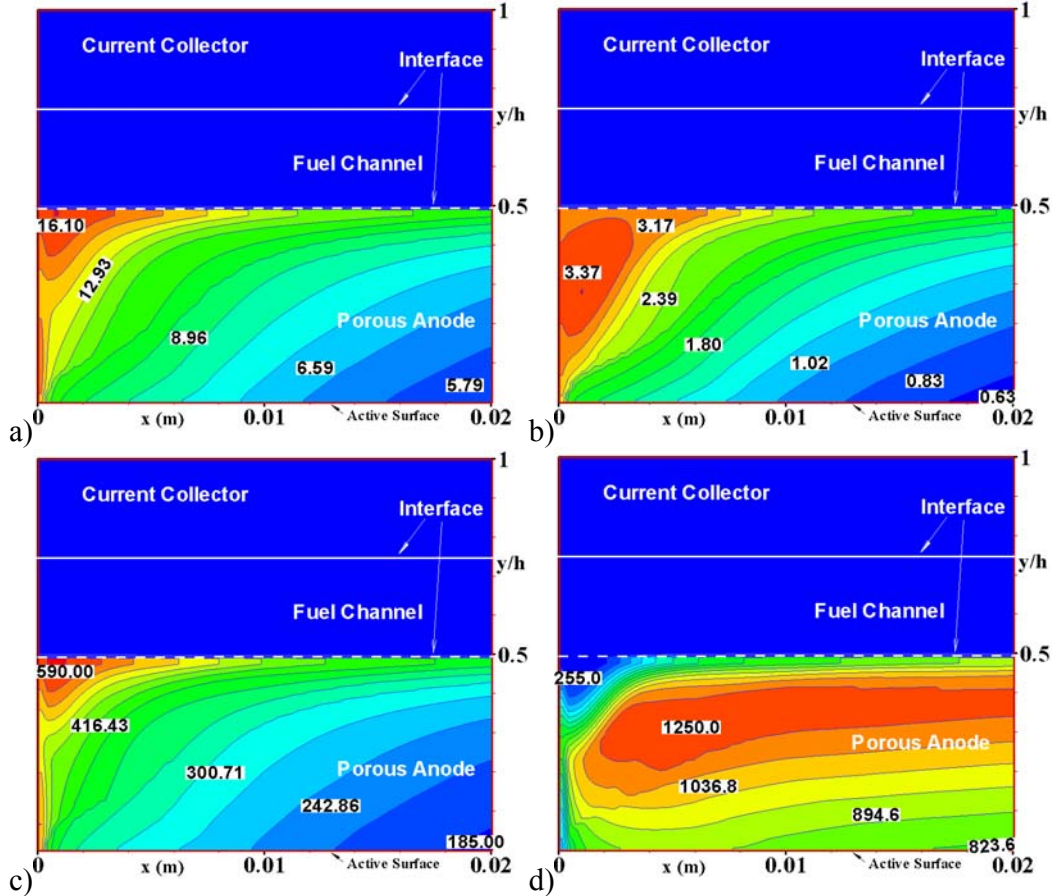
Figure 5. Distribution of catalytic reaction rates for the gas-phase species: a) H_2; b) CH_4; c) H_2O; and d) CO along main flow direction of an ITSOFC anode.

The dominating catalytic reforming reaction rates are shown in Fig. 5. It is found that the surface reactions for the gas-phase species are strong at the interface and the entrance regions within the porous layer close to the fuel flow channel (with big reaction rate value), except the one shown in Fig. 5d for CO. Decreased reaction rates can be observed in the rest of the porous anode, particularly after a certain distance downstream the inlet and close to the TPB. The distance for this specific case is about half the anode length. On the other hand, the reaction rate for CO holds the biggest values in the central part of the porous anode deep from the interface between the fuel channel and the porous anode. This is reflected as well by big values of CO mass concentration in Fig. 4a.

Figure 6 shows the surface coverage of dominating surface-phase species in the porous anode. It is found in Fig. 6a that there are more free Ni_s surfaces at the inlet regions close to the interface between the fuel channel and the porous anode, i.e., the Ni_s surfaces are relatively open. It is also true that the free Ni_s surfaces decrease along the main flow direction and towards the active TPB. On the other hand, surface coverage of H_s becomes big along with the catalytic reactions in both the main flow direction and deep into the porous anode. This is so because the surface coverages of H_s can result from the dissociative adsorption of the gas-phase species H_2O and CH_4.
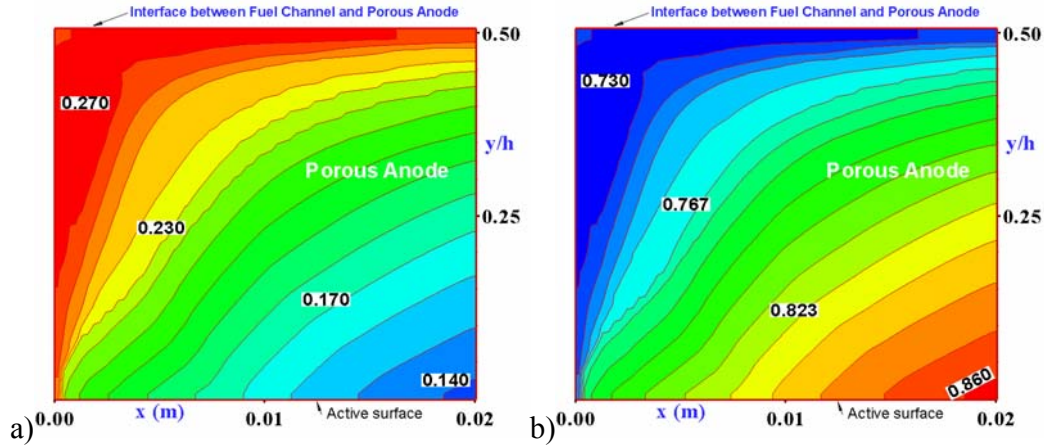
Figure 6. a) Fraction of Ni_s vacancies; and b) surface coverage of H_s along main flow direction of an ITSOFC anode.
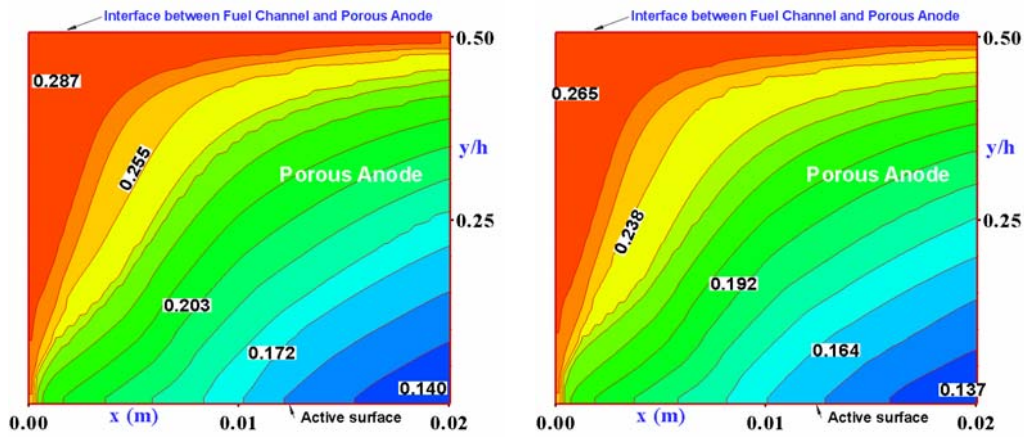
Figure 7. Fraction of Ni_s vacancies at temperature at: a) 700^oC; and b) 900^oC along main flow direction of an ITSOFC anode.

Figure 8. Surface coverage of H_s at: a) 700^oC; and b) 900^oC along main flow direction of an ITSOFC anode.

To understand the role of operating temperature on the catalytic reactions simulations are carried out for various parameters. A comparison of the fraction of Ni_s free sites and the surface coverage of

11

H_s are shown in Figs. 7 and 8, respectively. It is found that a higher operating temperature at 900°C results in a smaller fraction of Ni_s free sites, and consequently a bigger surface coverage of H_s, if Figs. 7b and 8b are compared with the ones shown in Figs. 7a and 8a, respectively. It is also clear that this change is stronger in the inlet region close to the interface than in the exit region close to the active TPB. For instance, the surface coverage of H_s changes between 0.734 and 0.713 in the inlet region, compared to the range of 0.862 to 0.859 in the exit region close to the TPB.
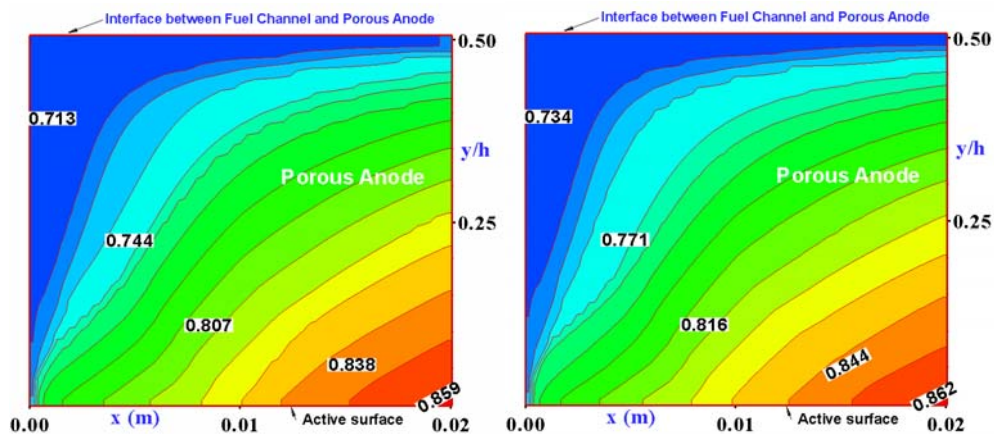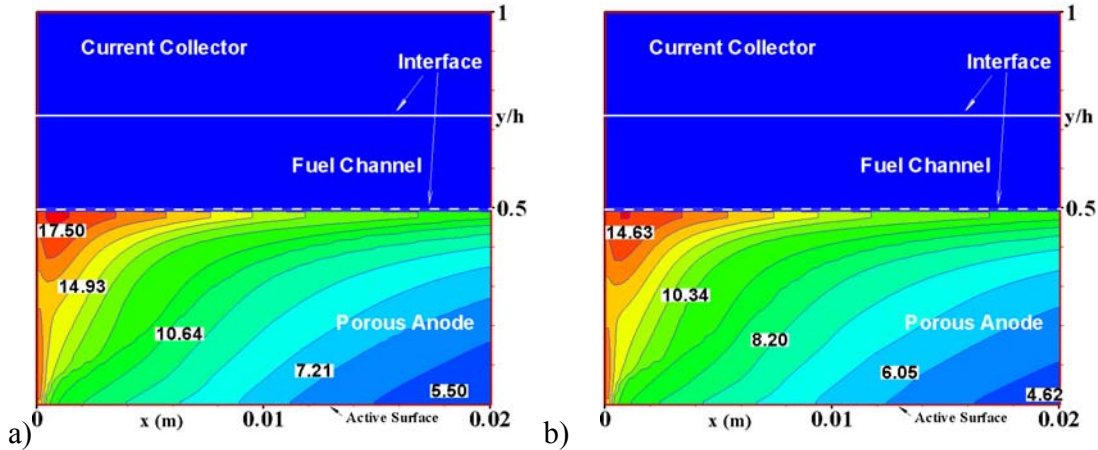

Figure 9. CH_4 reaction rate at operating temperature of: a) 700°C; and b) 900°C along main flow direction of an ITSOFC anode.

The temperature effects on the catalytic reactions are shown in Fig. 9 for the gas-phase species CH_4. It is a fact that a higher operating temperature results in a smaller reaction rate. This is evident if Fig. 9b is compared with Fig. 9a. However the reduction in the catalytic reaction rate is minor in the exit region close to the TPB, if compared to the one in the inlet region close to the interface. As expected, less H_2 are generated and its mass fraction is small at the higher temperature. However, this change in Fig. 10 is in a minor range, i.e., the operating temperature holds more significant effects on the catalytic reactions than on the gas-phase species transport processes.
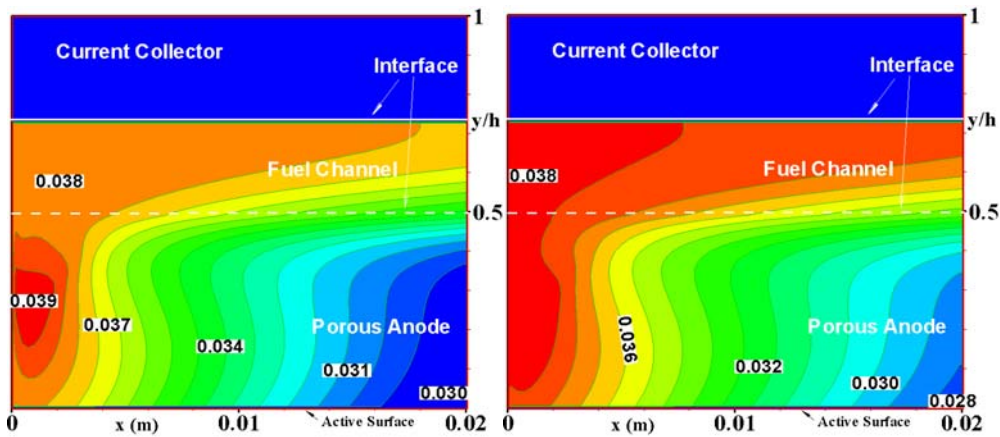
Figure 10. H_2 mass fraction profiles at operating temperature of: a) 700°C; and b) 900°C along main flow direction of an ITSOFC anode.

Parameter studies are also conducted for the porous anode permeability to reveal its effects on the catalytic reactions and further on the transport processes. As shown in Fig. 11b, increasing the permeability results in a big fraction of Ni_s free sites for the catalytic reactions, compared to the one

shown in Fig. 11a. However, this effect is limited in the inlet region, compared to that in the exit region close to the TPB. Consequently big catalytic reaction rates are expected for the gas-phase species. For instance, comparison of the reaction rates for CH_4 is shown in Fig. 12. It is true that in Fig. 12b a stronger effect can also be found in the exit region close to the TPB, when the porous anode permeability is big.

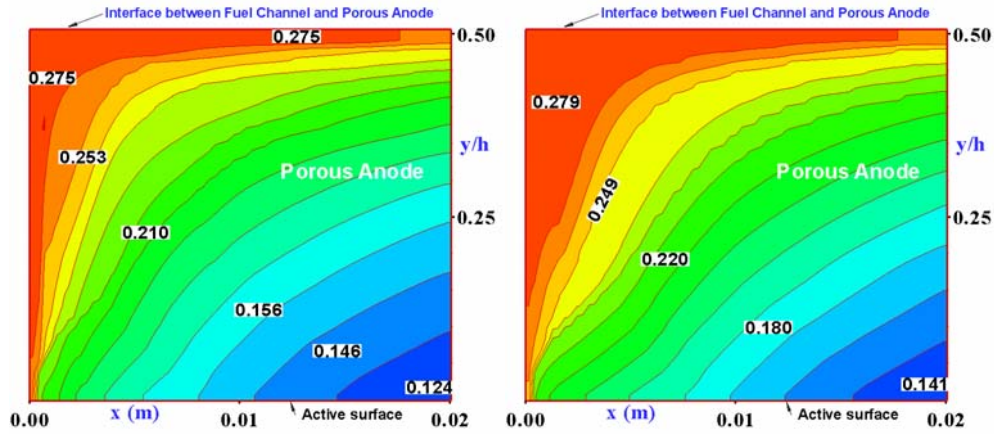Figure 11. Fraction of Ni_s vacancies for permeability β: a) 2×10^{-11} m^2; and b) 2×10^{-9} m^2 along main flow direction of an ITSOFC anode.

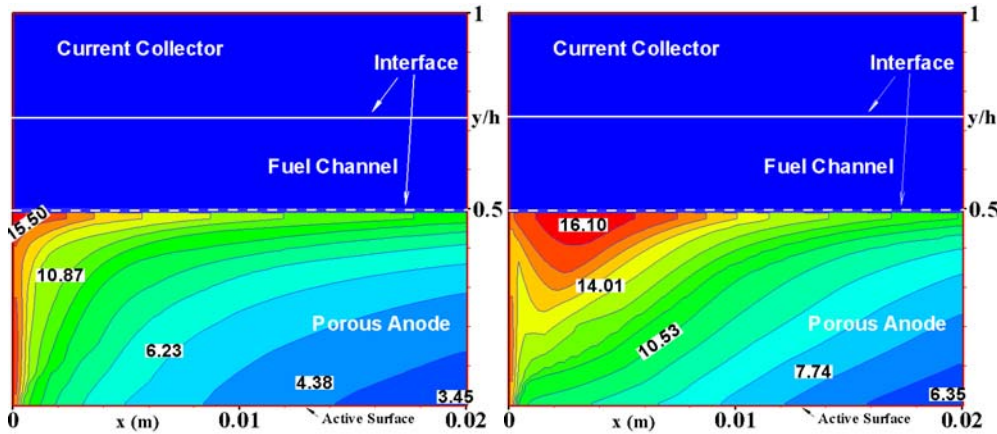Figure 12. Permeability effects on CH_4 reaction rate at β: a) 2×10^{-11} m^2; and b) 2×10^{-9} m^2 along main flow direction of an ITSOFC anode.

It is noted from Fig. 13b that, by increasing the permeability, the gas-phase species H_2 permeation to the porous layer is significant, i.e., inlet H_2 composition can be found in a quite big area in the porous anode close to the fuel channel, if compared to the case with a small permeability shown in Fig. 13a. It is also found that the catalytic surface reaction happens deeply in the porous anode in Fig. 12b, if compared with the case shown in Fig. 12a for a small permeability. As for this case, better utilization of catalytic surfaces in the porous anode can be expected, which can be verified by the CH_4 distribution in Fig. 9a. This is so because the permeability is a term used for the conductivity of the porous medium with respect to permeation by gas-phase species. It is known that a big permeability of a porous layer allows more gas to pass at the same pressure gradient. Consequently, more gas species is permeated from the fuel channel, and the gas convection can be found with bigger velocities in the porous layer close to the fuel flow channel at the entrance region. Certain impacts on the change of the axial velocity distribution are expected for both the fuel flow

13

channel and the porous anode layer, when the permeability is big. These effects are shown in Fig. 14 for the fuel gas velocity distribution.
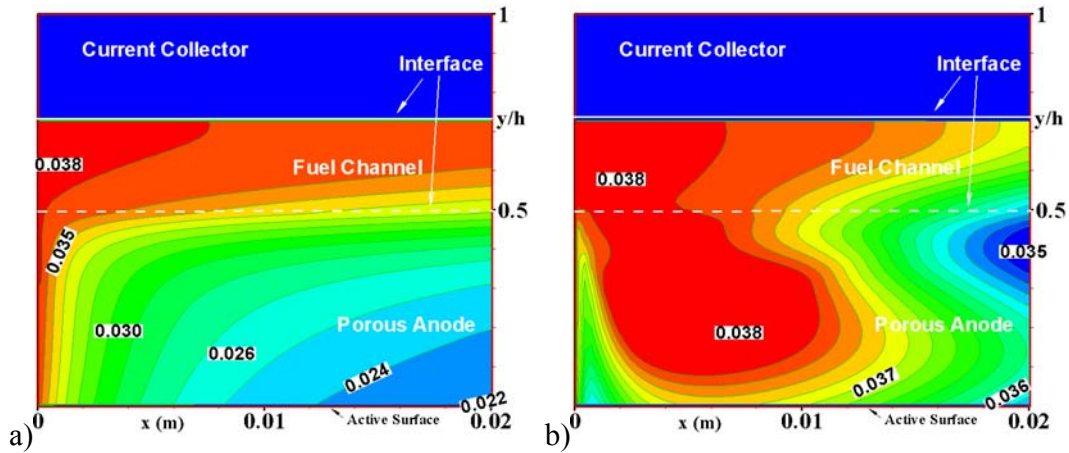
Figure 13. Permeability effects on H_2 mass fraction distribution at β: a) 2×10^{-11} m^2; and b) 2×10^{-9} m^2 along main flow direction of an ITSOFC anode.
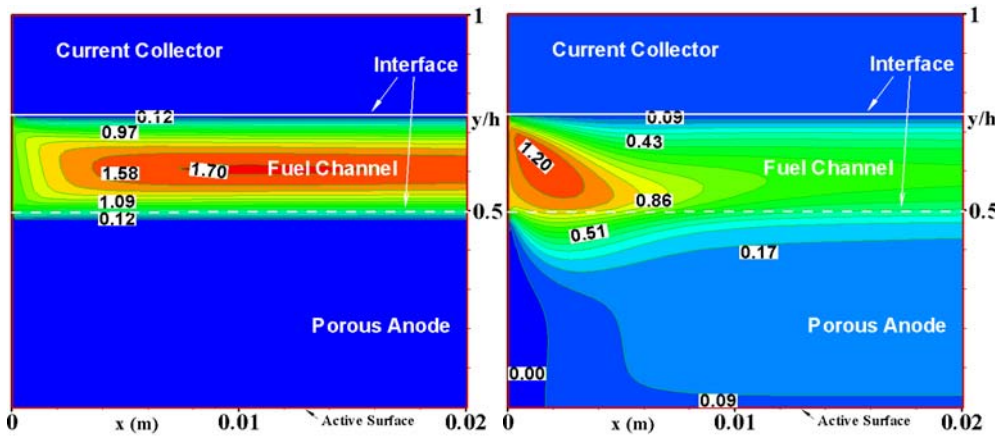

Figure 14. Fuel gas flow velocity distribution at β: a) 2×10^{-11} m^2; and b) 2×10^{-9} m^2 along main flow direction of an ITSOFC anode.
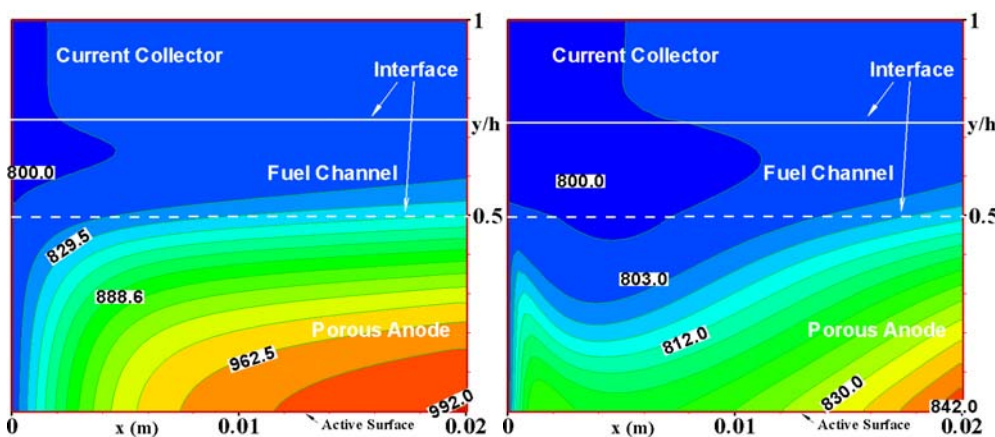

Figure 15. Temperature distribution profiles at β: a) 2×10^{-11} m^2; and b) 2×10^{-9} m^2 along main flow direction of an ITSOFC anode.

As shown in Fig. 15, the variation in temperature distribution can be observed in both the vertical and main flow direction with a slightly larger value close to TPB. These are created by the heat generation due to the electrochemical reactions close to the active surface. It is also found that the anode employing small permeability have high temperatures in both the fuel flow channel and the porous anode. For instance, the maximum temperature appearing in the active surface corner at the exit is 992°C in Fig. 15a, compared to 842°C for the case with big permeability (Fig. 15b). It is so because the steam reforming reaction is stronger and more deeply penetrated into the porous anode (as in Fig. 12), the more heat is then consumed when the permeability is big.

5. CONCLUSIONS

A three-dimensional CFD approach has been developed to analyze the chemical-reaction-coupled gas flow and heat transfer processes in a composite anode domain in intermediate temperature planar design SOFCs. Momentum and heat transport together with gas-phase species equations are solved by coupled source terms, variable thermo-physical and transport properties of the fuel gas species. A detailed multi-step heterogeneous steam reforming reaction scheme is implemented for the microscopic catalytic reactions to account for the steam reforming, the water-gas shift reforming and Boudouard reactions.

The predicted results show that the catalytic reactions take place at most regions of the porous anode, and a gradual CH_4 distribution profile and incomplete CH_4 conversion at the anode exit are found. This finding differs from those by typical CH_4 and H_2O consumption profiles obtained by global reforming schemes [16]. The similar conclusions have been reported by the developers of the reaction mechanism and other investigators. Transport processes of the fuel gas species and temperature distribution are affected by both the internal reforming reactions and the electrochemical reaction. Parameter studies show that both low operating temperature and big permeability can increase the available nickel surface fraction in the anode. Such detailed reaction scheme is much more complicated to incorporate in SOFC modelling but helpful to predict surface-phase species profiles over Ni-catalyst surfaces.

ACKNOWLEDGEMENTS

REFERENCES

[1] Wang, W.G. and Mogensen, M. (2005). High-performance Lanthanum-ferrite-based cathode for SOFCs. *Solid State Ionics* 176: 457-462.

[2] Hussain, M.M., Li, X., and Dincer, I. (2006). Mathematical Modeling of Planar Solid Oxide Fuel Cells. *Journal of Power Sources* 161:1012-1022.

[3] Virkar, A.V., Chen, J., Tanner, C.W. and Kim, J.W. (2000). The Role of Electrode Microstructure on Activation and Concentration Polarizations in Solid Oxide Fuel Cells. *Solid State Ionics* 131:189-198.

[4] Yakabe, H., Hishinuma, M., Uratani, M., Matsuzaki, Y. and Yasuda, I. (2000). Evaluation and Modeling of Performance of Anode-supported Solid Oxide Fuel Cell. *J. Power Sources* 86: 423-431.

[5] Lehnert, W., Meusinger, J. and Thom, F. (2000). Modelling of Gas Transport Phenomena in SOFC Anodes. *J. Power Sources* 87:57-63.

[6] Ackmann, T., Haart, L.G.J., Lehnert, W. and Thom, F.. Modelling of Mass and Heat Transport in Thick-Substrate Thin-Electrolyte Layer SOFCs. *Proc. 4th European Solid Oxide Fuel Cell Forum 2000*, Lucerne/Switzerland, 431-438.

[7] Yuan, J., Rokni, M. and Sundén, B. (2003). Three-Dimensional Computational Analysis of Gas and Heat Transport Phenomena in Channels Relevant for Anode-Supported Solid Oxide Fuel Cells. *Int. J. Heat Mass Transfer* 46:809-821.

[8] Yakabe, H., Ogiwara, T., Hishinuma, M. and Yasuda, I. (2001). 3-D Model Calculation for Planar SOFC, *J. Power Sources* 102:144-154.

[9] Barzi, Y.M., Ghassemi, M., Hamedi, M.H. and Afshari, E (2007). Numerical Analysis of Output Characteristics of a Tubular SOFC with Different Fuel Compositions and Mass Flow Rates. In: Proceedings of *Solid Oxide Fuel Cells 10 (SOFC-X)*, Eguchi, K., Singhal, S.C., Yokokawa, H. and Mizusaki, J. (eds.). ECS Transactions, 7: 1919-1928.

[10] Yuan, J. and Sundén, B., (2006). Analysis of Chemically Reacting Transport Phenomena in an Anode Duct of Intermediate Temperature SOFCs, *ASME J. Fuel Cell Sci., Tech. and Engn.*, 2: 89-98.

[11] Aguiar, A., Adjiman, C.S. and Brandon, N.P. (2004). Anode-supported Intermediate Temperature Direct Internal Reforming Solid Fuel Cell. I: Model-based Stead-state Performance. *J. Power Sources* 138:120-136.

[12] Hecht, E.S., Gupta, G.F., Zhu, H., Dean, A.M, Kee, R.J., Luba, M. and Deutschmann, O. (2005). Methane Reforming Kinetics within a Ni-YSZ SOFC Anode Support, *Appl. Catalysis A: General* 295: 40-51.

[13] Janardhanan, V.M. and Deutschmann, O. (2006). CFD Analysis of a Solid Oxide Fuel Cell with Internal Reforming: Coupled Interactions of Transport of Transport, Heterogeneous Catalysis and Electrochemcial Processes, *J. Power Sources* 162:1192-1202.

[14] Hofmann, P., Panopoulos, K.D., Fryda, L.E. and Kakaras, E. (2009). Comparison between Two Methane Reforming Models Applied to a Quasi-two-dimensional Planar Solid Oxide Fuel Cell Model, *Energy*, in press.

[15] Hecht, E.S., Gupta, G.K., Zhu, H., Dean, A.M., Kee, R.J., Maier, L and Deutschmann, O. (2005). Methane Reforming Kinetics within a Ni–YSZ SOFC Anode Support, *Applied Catalysis A: General* 295:40-51.

[16] Yuan, J., Yang, G., Andersson, M. and Sundén, B., (2008). CFD Approach for Chemical Reaction Coupled Heat Transfer in SOFCs, in Proceedings of *7th International Symposium on Heat Transfer* (cd-rom), 2008, Beijing, China.

[17] Mostinsky, I.L., "Diffusion coefficient," in: *International Encyclopedia of Heat & Mass Transfer*, Hewitt, G.F., Shires, G.L. and Polezhaev, Y.V. (eds.), 1996, CRC Press, Florida, USA.

NOMENCLATURE

A Arrhenius parameters for the rate constants, moles, cm, and s
A_{active} surface area of control volume at active site, m^2
a width of porous layer, m
B inertial coefficient
b width of flow channel, m
c_p specific heat capacity,   J/(kg K)
D molar diffusion coefficient of gas-phase species, m^2/s
E_a activation energy, kJ/mol
H enthalpy, kJ/mol
h overall height of the channel, m
h_d height of the channel, m
h_p thickness of porous layer, m

ITSOFC   intermediate temperature solid oxide fuel cell
J electrochemical reaction related molar flux, mol/(m^2 s)
K number of species, -
K_e equilibrium constants, Pa^2
k thermal conductivity, W/(m K); reaction rate constant, mol/(m^3 Pa^2 s) and mol/(cm^2 s)
k_0 pre-exponential constant, -
M molecular weight of species, kg/mol
$\dot{m}$ mass diffusion flux, kg/(m^2 s)
$\dot{n}$ molar diffusion flux, mol/(m^2 s)
n total number of gas-phase species, -
P pressure, Pa
q heat flux, W/(m^2)
R reaction rate, mol/(m^{3}s); desorption/adsorption rate, mol/(cm^2 s)
$\Re$ gas constant, kJ/(mol K)
Re Reynolds number (UD$_h$/ν), -
r_e effective radius, m
S source term
SOFC solid oxide fuel cell
T temperature, ^{o}C
v stochiometric coefficients, -
V   velocity vector, m/s
V_i velocity components in x, y and z directions, respectively, m/s
X molar fraction of fuel species, -
Y mass fraction of fuel species, -
x, y, z Cartesian coordinates
$[X]$ surface-phase species concentration, mol/cm^2; gas-phase species concentration, mol/cm^3
YSZ   yttria stabilized zirconia

Greek Symbols

β permeability of porous layer, m^2
Γ_{tot} total surface site density, mol/cm^2
ε porosity, -;
θ surface site fraction, -
μ dynamic viscosity, kg/(m s)
ν kinematic viscosity, m^2/s
ρ density, kg/m^3
τ tortuosity, -

Superscripts

+   forward reaction
-        reverse reaction

Super- and subscripts

ad   adsorption
di   diffusion layer
eff   effective parameter
f   fuel gas mixture
CH$_4$ methane
CO   carbon monoxide

CO_2 carbon dioxide
des   desorption
e   equilibrium
g   gas-phase species
gm   fuel gas mixture
H_2 hydrogen
H_2O water
in   inlet
k   Knudsen diffusion
m   mass transfer
p   permeation
r   steam reforming reaction
s   solid wall; shift reaction; species; surface-phase species

Appendix A: Heterogeneous reaction mechanism for methane reforming on Ni/YSZ [15].

	Reaction	A [a]	n	E [a]
1	$H_2 + Ni_s + Ni_s \rightarrow H_s + H_s$	1.000×10^{-02} [b]	0.0	0.00
2	$H_s + H_s \rightarrow Ni_s + Ni_s + H_2$	$5.593 \times 10^{+19}$	0.0	88.12
3	$O_2 + Ni_s + Ni_s \rightarrow O_s + O_s$	1.000×10^{-02} [b]	0.0	0.00
4	$O_s + O_s \rightarrow Ni_s + Ni_s + O_2$	$2.508 \times 10^{+23}$	0.0	470.39
5	$CH_4 + Ni_s \rightarrow CH_{4s}$	8.000×10^{-03} [b]	0.0	0.00
6	$CH_{4s} \rightarrow Ni_s + CH_4$	$5.302 \times 10^{+15}$	0.0	33.15
7	$H_2O + Ni_s \rightarrow H_2O_s$	1.000×10^{-01} [b]	0.0	0.00
8	$H_2O_s \rightarrow Ni_s + H_2O$	$4.579 \times 10^{+12}$	0.0	62.68
9	$CO_2 + Ni_s \rightarrow CO_{2s}$	1.000×10^{-05} [b]	0.0	0.00
10	$CO_{2s} \rightarrow Ni_s + CO_2$	$9.334 \times 10^{+07}$	0.0	28.80
11	$CO + Ni_s \rightarrow CO_s$	5.000×10^{-01} [b]	0.0	0.00
12	$CO_s \rightarrow Ni_s + CO$	$4.041 \times 10^{+11}$	0.0	112.85
		ε_{CO_s}		−50.0 [c]
13	$O_s + H_s \rightarrow OH_s + Ni_s$	$5.000 \times 10^{+22}$	0.0	97.90
14	$OH_s + Ni_s \rightarrow O_s + H_s$	$2.005 \times 10^{+21}$	0.0	37.19
15	$OH_s + H_s \rightarrow H_2O_s + Ni_s$	$3.000 \times 10^{+20}$	0.0	42.70
16	$H_2O_s + Ni_s \rightarrow OH_s + H_s$	$2.175 \times 10^{+21}$	0.0	91.36
17	$OH_s + OH_s \rightarrow O_s + H_2O_s$	$3.000 \times 10^{+21}$	0.0	100.00
18	$O_s + H_2O_s \rightarrow OH_s + OH_s$	$5.423 \times 10^{+23}$	0.0	209.37
19	$O_s + C_s \rightarrow CO_s + Ni_s$	$5.200 \times 10^{+23}$	0.0	148.10
20	$CO_s + Ni_s \rightarrow O_s + C_s$	$1.418 \times 10^{+22}$	−3.0	115.97
		ε_{CO_s}		−50.0 [c]
21	$O_s + CO_s \rightarrow CO_{2s} + Ni_s$	$2.000 \times 10^{+19}$	0.0	123.60
		ε_{CO_s}		−50.0 [c]
22	$CO_{2s} + Ni_s \rightarrow O_s + CO_s$	$3.214 \times 10^{+23}$	−1.0	86.50
23	$HCO_s + Ni_s \rightarrow CO_s + H_s$	$3.700 \times 10^{+21}$	0.0	0.0
		ε_{CO_s}		50.0 [c]
24	$CO_s + H_s \rightarrow HCO_s + Ni_s$	$2.338 \times 10^{+20}$	−1.0	127.98
25	$HCO_s + Ni_s \rightarrow O_s + CH_s$	$3.700 \times 10^{+24}$	−3.0	95.80
26	$O_s + CH_s \rightarrow HCO_s + Ni_s$	$7.914 \times 10^{+20}$	0.0	114.22
27	$CH_{4s} + Ni_s \rightarrow CH_{3s} + H_s$	$3.700 \times 10^{+21}$	0.0	57.70
28	$CH_{3s} + H_s \rightarrow CH_{4s} + Ni_s$	$4.438 \times 10^{+21}$	0.0	58.83
29	$CH_{3s} + Ni_s \rightarrow CH_{2s} + H_s$	$3.700 \times 10^{+24}$	0.0	100.00
30	$CH_{2s} + H_s \rightarrow CH_{3s} + Ni_s$	$9.513 \times 10^{+22}$	0.0	52.58
31	$CH_{2s} + Ni_s \rightarrow CH_s + H_s$	$3.700 \times 10^{+24}$	0.0	97.10
32	$CH_s + H_s \rightarrow CH_{2s} + Ni_s$	$3.008 \times 10^{+24}$	0.0	76.43
33	$CH_s + Ni_s \rightarrow C_s + H_s$	$3.700 \times 10^{+21}$	0.0	18.80
34	$C_s + H_s \rightarrow CH_s + Ni_s$	$4.400 \times 10^{+22}$	0.0	160.49
35	$O_s + CH_{4s} \rightarrow CH_{3s} + OH_s$	$1.700 \times 10^{+24}$	0.0	88.30
36	$CH_{3s} + OH_s \rightarrow O_s + CH_{4s}$	$8.178 \times 10^{+22}$	0.0	28.72
37	$O_s + CH_{3s} \rightarrow CH_{2s} + OH_s$	$3.700 \times 10^{+24}$	0.0	130.10
38	$CH_{2s} + OH_s \rightarrow O_s + CH_{3s}$	$3.815 \times 10^{+21}$	0.0	21.97
39	$O_s + CH_{2s} \rightarrow CH_s + OH_s$	$3.700 \times 10^{+24}$	0.0	126.80
40	$CH_s + OH_s \rightarrow O_s + CH_{2s}$	$1.206 \times 10^{+23}$	0.0	45.42
41	$O_s + CH_s \rightarrow C_s + OH_s$	$3.700 \times 10^{+21}$	0.0	48.10
42	$C_s + OH_s \rightarrow O_s + CH_s$	$1.764 \times 10^{+21}$	0.0	129.08

[a] Arrhenius parameters for the rate constants.
[b] Sticking coefficient.
[c] Coverage-dependent activation energy.